Phys. Med. Biol. **56** (2011) 1259–1279 doi:10.1088/0031-9155/56/5/003

Cone-beam optical computed tomography for gel dosimetry II: imaging protocols

Tim Olding[1] **and L John Schreiner**[1,2]

[1] Department of Physics, Queen's University, Kingston, Ontario K7L3N6, Canada
[2] Cancer Centre of South Eastern Ontario at Kingston General Hospital, 25 King Street West, Kingston, Ontario K7L5P9, Canada

E-mail: tim.olding@krcc.on.ca

Received 5 August 2010, in final form 3 December 2010
Published 1 February 2011
Online at stacks.iop.org/PMB/56/1259

Abstract

This work develops imaging protocols for improved dose readout of a Fricke-xylenol orange-gelatin (FXG) gel-filled 1 L polyethylene terephthalate (PETE) jar dosimeter using a commercial Vista^{TM} cone-beam optical computed tomography (CT) scanner from Modus Medical Devices Inc. (London, ON, Canada). To ensure good management of light source–detector stability, it was determined that (a) a minimum of 2 h warm-up time is necessary prior to dosimeter scanning, (b) the light source should be kept on until the completion of the last data scan except for the minimum amount of time required to acquire dark field images, and (c) the optional Vista software projection image normalization routine should be used in image reconstruction. The institution of dosimeter scan time and temperature control was strongly indicated from the experiments. A standard post-irradiation wait time of 30 min measured to within ± 30 s was established to minimize the measurement uncertainties due to dosimeter development and diffusion. To alleviate thermochromic behavior leading to inaccurate dose readout, holding bath warm up and pre-scan temperature adjustment procedures were developed to control dosimeter temperature to within ± 0.2 °C. The possibility of stray light minimizing protocols was also investigated and deemed to be unnecessary. The largest significant sources of stray light in the system were identified as being due to angled scatter from the dosimeter gelatin matrix and refraction from the jar wall interfaces. It was concluded that these phenomena would be better addressed through dosimeter modification and an inter-jar dose-to-attenuation calibration methodology, rather than by setting additional imaging protocols.

1. Introduction

Since the emergence of gel dosimetry as a potential candidate for three-dimensional (3D) dose measurements in radiation therapy (Gore *et al* 1984, Olsson *et al* 1990), significant attention has been directed toward the use of magnetic resonance imaging (MRI) for gel dosimeter readout (Schreiner and Olding 2009). One reason for MRI being quickly established as the preferred modality for 3D dose readout was its prior development as a mature technology in other medical applications, which served as a good basis for the new task of gel dosimetry (Doran 2009).

The preferred dose contrast mechanism in MRI of gel dosimeters has typically been the change in R2 spin–spin relaxation rate, which can be calibrated to obtain a quantitative 3D dose distribution from the irradiated gel dosimeter (Baldock *et al* 1998, 1999, Taylor *et al* 2007, 2009). However, there was some confusion in the early development of this field, which, in part, was occasioned by the lack of standard protocols for MRI (Schreiner and Olding 2009). Following this early work were some investigations aimed toward the optimization of MRI parameters for gel dosimetry (De Deene and Baldock 2002, De Deene 2004), which helped to bring better consistency to the field. Other studies focused on a variety of other factors, such as dosimeter temperature at irradiation, post-irradiation time before scanning, and dosimeter temperature at time of scanning for different types of normoxic polymer gel (De Deene *et al* 2002, 2006). From these studies, a number of recommendations have been developed (i.e. imaging protocols) for good practice in MRI-based gel dosimetry.

In the mid-1990s, optical computed tomography (CT) was introduced as an alternative 3D readout method for gel dosimeters (Tarte and van Doorn 1993, 1995, Gore *et al* 1996). Unlike MRI, optical CT had not seen significant prior development as a quantitative 3D imaging tool, and to date, much important characterization work remains to be done in this field. A number of scanner designs have been introduced since then, ranging from improved translate–rotate scanners (Krstajic and Doran 2007b, Lopatiuk-Tirpak *et al* 2008) to faster area detection schemes (as opposed to point detection) based on cone-beam (Wolodzko *et al* 1999, Babic *et al* 2008) and parallel-beam (Doran *et al* 2001, Krstajic and Doran 2006, 2007a) charge-coupled device (CCD) configurations. Each of these approaches to data acquisition has advantages and limitations that need to be understood and characterized in combination with the chemistry of the gel dosimeter in use.

In a previous work, some basic properties of the Vista^{TM} cone-beam optical CT scanner (Modus Medical Devices Inc.) were characterized (Olding *et al* 2010) and the scanner shown to be capable of imaging optically absorbing media to the Resolution, imaging Time, Accuracy and Precision (RTAP) criteria that have been suggested for comparing the imaging modalities of MRI and optical CT (Oldham *et al* 2001). The experimental investigations presented in this paper follow up on imaging issues raised in Olding *et al* (2010), and are particularly directed at improving the accuracy of cone-beam optical CT imaging of a Fricke-xylenol orange-gelatin (FXG) gel dosimeter (Kelly *et al* 1998). This dosimeter has previously been shown to be well suited for use with optical cone-beam imaging (Babic *et al* 2008, 2009) since it benefits from optical absorption being its contrast mechanism. In addition to establishing some of the necessary details for reliable cone-beam optical imaging of an FXG gel dosimeter, this paper is intended to serve as an illustrative example of the work that is required to move past basic scanner characterization to imaging a specific type of gel dosimeter with its own inherent strengths and limitations. As in Olding *et al* (2010), basic assessments are completed employing calibration scattering solutions, absorbing solutions, and gelatin phantoms that allow the optical measurement to be separated from the uncertainties in dose delivery and gel dosimetry. Time and temperature imaging protocols are established for improved dosimeter

readout. The main sources of stray light perturbation in the system are then assessed and recommendations made for future improvement in the optical measurement of 3D dose.

2. Experiment

This section starts with a general overview of the preparation and imaging of calibration solutions and FXG gel dosimeters. The first set of experiments is directed at setting a scanner-related protocol for improving measurement accuracy. Then, time and temperature-related attenuation variations in the FXG gel are investigated in order to establish corresponding dosimeter-related protocols. The final set of experiments is aimed at understanding the sources of stray light perturbation in the system, and in this case, the investigations of the dosimeter- and scanner-related stray light sources are discussed together.

2.1. Cone-beam optical CT imaging

Three-dimensional imaging was performed using a Vista cone-beam optical scanner (Modus Medical Devices Inc.) employing a charged-coupled device (CCD) camera with the lens aperture set to f5, and either 633 or 590 nm LED diffuse light panel illumination (specified in each experiment). As a detailed description of the scanner and its operation has previously been reported (Olding *et al* 2010), only necessary details are repeated here. A matching tank solution for the scanner consisted of 10–12 wt% propylene glycol (cat. no 134368, Sigma-Aldrich Ltd, Oakville, Canada) in water, the refractive index of which (1.344–1.346 $\pm$ 0.001 at 590 nm) was monitored over time at room temperature (21 $\pm$ 1 °C) using a handheld refractometer with a central measurement wavelength of 589 nm (r^2 mini refractometer, Reichert Analytical Instruments, Depew, NY, USA). A minimal change in the tank solution index on the order of -0.0001 °C^{-1} was observed as the temperature was increased over the range of 15–25 °C. Temperature measurements were taken using a digital temperature probe (TM99A-NA Digital Thermometer, Nuclear Associates, Carle Place, NY, USA). For each scan, a set of 410 light intensity transmission projections was acquired over 360° in approximately 4 min. Reference scans were completed on a 1 L PETE jar containing a matching tank solution (or on an FXG gel-filled 1 L PETE dosimeter jar prior to irradiation) at the highest shutter exposure time possible without inducing camera pixel saturation and with the lowest gain setting. Data scans were acquired at the same camera settings as the reference scan in all of the imaging runs. Optical CT attenuation images were reconstructed to an isotropic voxel resolution of 0.5 or 1.0 mm. The default resolution was 0.5 mm, unless otherwise specified.

The calibration scattering solutions, absorbing solutions, and uniform 5 wt% gelatin-in-water phantoms used for investigating the possibility of standard imaging protocols were prepared according to Olding *et al* (2010). FXG gel dosimeters in this work were prepared according to the recipe suggested by Babic *et al* (2008), containing 0.3 mM ferrous ammonium sulfate (cat. no 203505, Sigma-Aldrich Ltd, Oakville, Canada), 0.05 mM xylenol orange (cat. no 398187, Sigma-Aldrich Ltd), 65 mM sulfuric acid (cat. no 258105, Sigma-Aldrich Ltd), and 6 wt% gelatin (300 bloom Type A porcine gelatin, cat. no G2500, Sigma-Aldrich Ltd) in distilled, de-ionized water. After preparation, the heated FXG solutions were poured into 1 L PETE jars and allowed to set overnight at 4 °C in a refrigerator.

Line profiles and regions of interest (ROI) in absorbing, scattering, gelatin phantom and FXG dosimeter projection data and optical CT reconstructed 3D data sets were evaluated using ImageJ (National Institute of Health, Bethesda, MD, USA), Microview 2.1.2 (GE Healthcare, UK) or MatLab (Mathworks, Newark, NJ, USA) software.

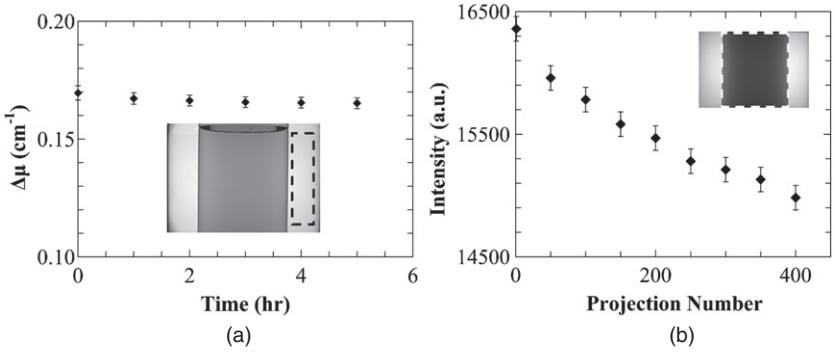

Figure 1. (a) Change in mean ROI attenuation of a uniform 0.10 g L^{-1} scattering solution with scanner warm up time. A slight drop is observed even with the use of a normalization region in the scan projection data (see the inset). (b) Variation in the mean jar region projection intensity (see the inset) observed in the first data scan of the 0.1 g L^{-1} calibration scattering solution.

2.2. Scanner light source–detector stability

One of the key requirements for achieving a high precision Vista scanner measurement is to ensure that the light source–detector combination yields a stable signal over time. A default projection image normalization region is employed by the cone-beam reconstruction software toward this end (figure 1(*a*) inset). In the software routine, a mean projection intensity value is calculated in the normalization region of interest (ROI) for each reference and data projection image. The set of mean intensity ROI values for each scan is averaged to obtain a mean scan intensity value for each scan. The reference and data projection image sets are then divided by their respective global scan normalization value to account for any light source–detector variability at the time of image collection.

To test the efficacy of this method of managing light source–detector variability, a reference scan was taken of a 1 L PETE jar containing 12 wt% propylene glycol-in-water matching tank fluid immediately after the scanner was turned on, under 633 nm illumination. Data scans of a 0.1 g L^{-1} calibration scattering solution were then acquired at 1 h intervals over a scanner warm-up period spanning 5 h. The results (figure 1(a)) indicate a 2.5% drop in mean attenuation over the 5 h period. Previous experiments have indicated that the most accurate region for dosimetry within the jar is a cylindrical ROI covering the central 8 cm of the jar's diameter (i.e. to within 5 mm of the jar wall) and the central 10 cm in height (Olding *et al* 2010). This cylindrical ROI was set as the evaluation volume for the data in figure 1(a).

Looking within the set of 410 projection images of the first data scan from figure 1(a), a significant drop in the mean 'jar region' projection intensity is clearly evident (figure 1(b)).

The open field intensity of the light source was subsequently evaluated over a 16 h time period using a photodiode detector (figure 2(a)) and was found to stabilize after approximately 2 h with the possibility of a slight sinusoidal ripple in magnitude over time. This ripple is observed from a sixth-order polynomial fit to the data (shown in figure 2(a)). The fit is ill-conditioned because of the significant spread in the data ($y = 0.000\,003x^6 - 0.0002x^5 + 0.0049x^4 - 0.0596x^3 + 0.3576x^2 - 0.9529x + 19.72$, $R^2 = 0.27$), but was felt to represent a real underlying phenomenon. A similar falloff in mean open field intensity was observed when using the scanner camera for the measurement of intensity (figure 2(b)). However, if the scanner light source was turned off for more than a few seconds, a sharp increase in mean

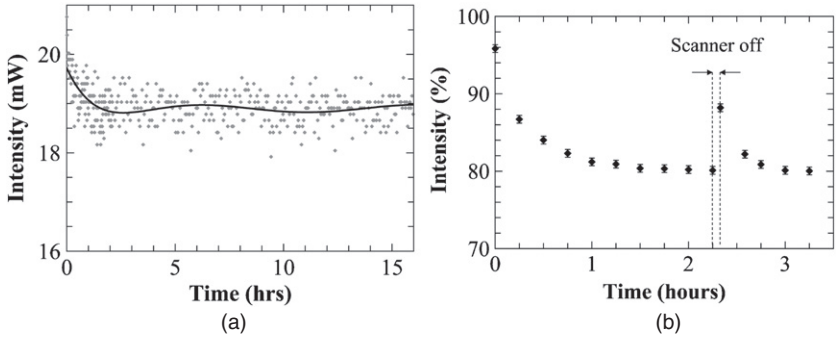

Figure 2. (a) An independent measurement of light source intensity over time using a photodiode detector indicates that the light source stabilizes in approximately 1–2 h. Error bars are smaller than the symbol size. (b) Mean open field intensity of the light source measured over time by the Vista scanner.

intensity was observed by the camera as the light source was turned on again (figure 2(b)), and the signal would then require additional time for stabilization.

2.3. Scan time constraints

Imaging FXG gel dosimeters, as opposed to scattering/absorbing solutions, involves additional time constraints beyond that of a scanner minimum warm up time. A previous report has indicated that the FXG dosimeter can stabilize in ∼40 min for a 200 cGy delivery (Kelly *et al* 1998), but a closer examination of the results from this work indicate that the attenuation is still increasing at a marginal rate of ∼3% per hour relative to the value obtained at the 40 min mark.

To investigate this further, an FXG gel dosimeter was irradiated to a superficial dose of 200 cGy on the day after manufacture using a Gulmay superficial x-ray therapy unit (Gulmay Medical Inc., Buford, GA, USA) with a 6 cm cone insert. The Gulmay unit was employed for the delivery in order to obtain a large variation in dose distribution within the gel volume. The dosimeter was then imaged on the Vista scanner at 590 nm multiple times over a 24 h period after irradiation. The dosimeter and the scanner matching tank fluid were held at $20.1 \pm 0.2\,^{\circ}$C during this post-irradiation time period. The central axis depth attenuation curves corrected for auto-oxidation effects (Babic *et al* 2008) clearly show dose development over this time period (figure 3(a)). Attenuation data taken from three depths in the curves and normalized to the attenuation value at a post-irradiation time of 30 min indicate an attenuation increase of approximately 2.8–3.0% per hour at each depth (figure 3(b)). An additional unpublished experiment completed by the authors has indicated that a similarly irradiated FX solution (without the gelatin, but with all other components present in the same percentages as usual) will stabilize in the mean attenuation value within 24 to 48 h under refrigeration, whereas the FXG gel will continue to react under refrigeration over a period of weeks (at a rate greater than that expected from auto-oxidation) to the point of response saturation. The role of gelatin in driving this reaction forward is not well understood and has not been investigated further to date.

Another factor that plays a role in the development of FXG dosimeter imaging protocols is the loss of spatial dose integrity over time due to diffusion of the ferric–xylenol orange ion complex (Harris *et al* 1996, Rae *et al* 1996, Baldock *et al* 2001). A line profile through the

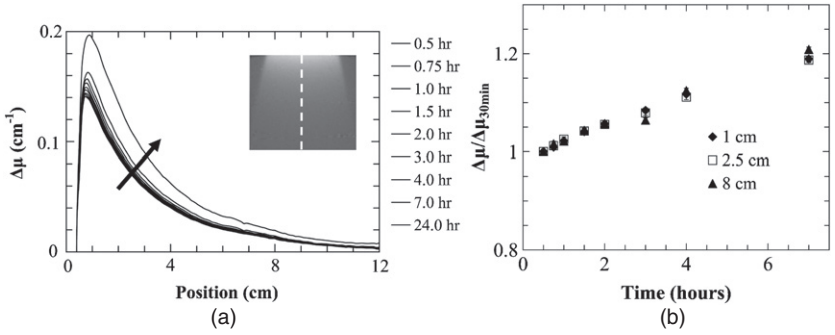

Figure 3. (a) Development of attenuation (depth dose) from an 80 kVp, 200 cGy, 6 cm cone Gulmay delivery. The arrow is directed toward increasing time. (b) Relative attenuation along the central axis at three positions along the central axis in the gel dosimeter (normalized to the attenuation value at 30 min). The error bars in (b) are smaller than the symbol size.

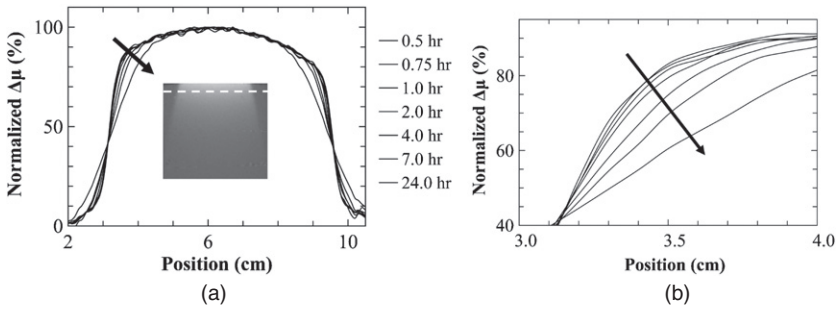

Figure 4. (a) Line profile through the central axis of the 200 cGy orthovoltage (80 kVp) delivery at 1 cm depth. Increasing time is indicated by the arrow direction. (b) A close-up view of the arrow region in (a).

optical CT image of the 200 cGy Gulmay delivery at a depth of 1 cm (figure 4(a), normalized to maximum attenuation) shows the effect of diffusion on spatial dose integrity over time. In an enlarged view near the top edge of the dose gradient (figure 4(b)), the normalized attenuation changes in magnitude at a rate up to ∼0.4% every 10 min at the fastest changing point along this attenuation (dose) profile.

2.4. Scan temperature constraints

Representative 0.1 g L^{-1} acrylic scattering and 1.48 mg L^{-1} patent blue violet dye absorbing solution-filled 1 L PETE jars were cooled in the refrigerator prior to optical scanning at 633 nm. The mean reconstructed ROI attenuation coefficient of the cooled scatter solution-filled jar was found to be elevated by slightly more than 3% compared to the room-temperature attenuation value. An evaluation of the mean transmitted intensity value within the jar region of the projection images indicates a slight trend of increasing intensity through the jar as it warms up (figure 5(a)). The measurements were repeated on the cooled absorbing solution, and less than 0.5% projection intensity variation was observed over the range of 10–21 °C (figure 5(a)).

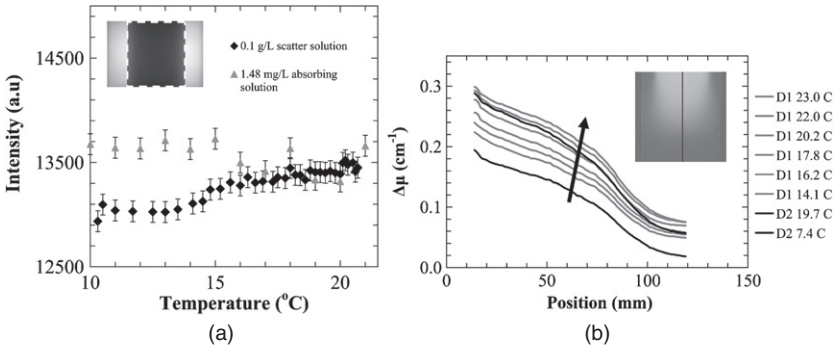

Figure 5. (a) Mean intensity of the open field projection data showing temperature dependence of uniform scattering acrylic and absorbing dye solutions. (b) Central axis attenuation for an FX gel dosimeter irradiated with a 200 cGy electron beam. Two sets of scans were obtained for this dosimeter on subsequent days (D1 in gray, D2 in black), with increasing temperature shown by the arrow direction.

The FXG gel dosimeter was assessed to see if the iron–xylenol orange dye complex had a similar temperature response to that of the patent blue violet dye. Figure 5(b) shows the reconstructed central axis attenuation (depth dose) for an FXG gel irradiated with a 6 × 6 cm, 20 MeV electron beam to a dose of 200 cGy at a reference depth of 3 cm, using a Varian Clinac 21iX linear accelerator (Varian Medical Systems, Palo Alto, CA, USA), and refrigerated for 3 weeks to ensure reaction completion (i.e. dosimeter development is minimal at this point). The measured dosimeter data are known to be inconsistent with the planned delivery due to diffusion effects over the 3 week post-irradiation time period. However, the primary interest is in obtaining relative data measurements at temperature, so this is not a significant issue. Individual scans were acquired at 590 nm on the Vista scanner and auto-oxidation effects were taken into account (Babic *et al* 2008). Temperature measurements at a single reference point in the dosimeter were taken prior to each scan by inserting the temperature probe 1 cm into the FXG gel. The temperature of the matching tank solution was held to 22 ± 1 °C during the scans. The dosimeter was placed in a covered, warm water-filled tank between scans. The dosimeter jar was then returned to the refrigerator and re-scanned on the following day. The scan data are shown in figure 5(b), with auto-oxidation effects between the 2 days accounted for in the data.

Some follow-up temperature experiments were then performed. An FX aqueous solution-filled 1 L PETE jar prepared according to Babic *et al* (2008), but not including the gelatin component, was irradiated through the top surface of the gel with an 1800 cGy, 6 × 6 cm, 6 MV photon beam (to the reference depth of 2 cm) and imaged at 590 nm and room temperature (21.4 ± 0.1 °C) at a post-irradiation time of 30 min. The jar was then cooled down in an ice bath and re-imaged over the next 2 h at different warm-up temperatures, with temperature readings taken in the same manner as for the data presented in figure 5(b). An FXG gel-filled 1 L PETE jar dosimeter was also prepared, irradiated with a 180 cGy, 6 × 6 cm, 6 MV photon beam, and similarly imaged. Mean ROI attenuation values for the region covering the central 8 cm in diameter and 10 cm in height of the imaged jars (reconstructed to 1 mm cubic voxel size) are shown in figure 6(a). Note that the uncertainties reported in figure 6(a) are related to the temperature measurement at the reference point and do not report the possibility of temperature variation throughout the jar media. The average uncertainty was assessed from slight positional changes in the visually approximated probe depth of 1 cm at different

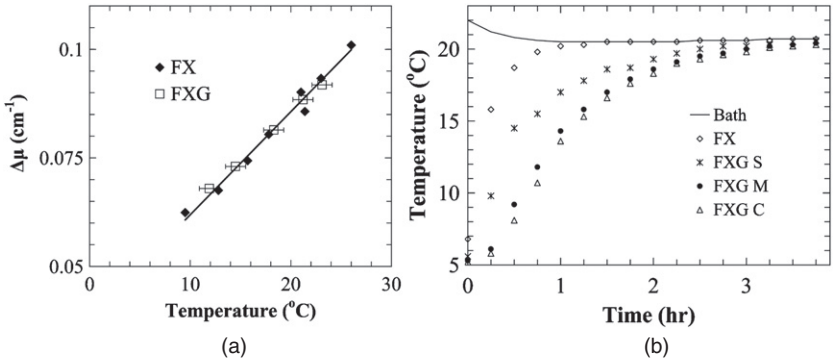

Figure 6. (a) Change in mean jar ROI attenuation values with temperature for (i) an FX solution-filled jar irradiated with an 1800 cGy 6 MV photon beam, and (ii) an FXG gel-filled jar irradiated with a 180 cGy 6 MV photon beam. (b) Temperature readings at the center of the FX jar, and at the center (C), mid-point along the radius (M), and side (S) of the FXG jar for a period of time after placing the refrigerated jars in a covered, 20 L warm-up bath. Some of the error bars are smaller than the symbol size.

temperatures, and was much smaller for the FX solution than for the FXG gel, presumably due to differences in diffusion. Finally, after overnight refrigeration, the two dosimeters were placed in a warm-up bath at 22 °C. Temperature readings were taken at 15 min intervals over a period of 4 h in the center of the FX jar (figure 6(b)). Temperature readings were also acquired at 15 min intervals over the same 4 h period at three points in the FXG jar with the probe inserted 9 cm deep into the FXG gel (also shown in figure 6(b)). The selected positions were located approximately 0, 2 and 4 cm from the center of the 4.6 cm radius jar.

2.5. Stray light reduction

Cone-beam optical CT imaging of absorbing and scattering solutions is known to be affected by optical artifacts due to stray light from a number of different sources (Jordan and Battista 2006, 2009, Bosi *et al* 2007, 2009, Olding *et al* 2010). Stray light perturbation occurs when light rays from the diffuse light source not originally traveling along a cone-beam primary ray path reflect or scatter onto that ray path (i.e. within some finite sized ray bundle defined primarily by the camera lens aperture), typically prior to exiting the attenuating media or when in transit through the camera lens optics. As light arriving along a primary ray path is indiscriminately focused onto the CCD chip regardless of the original path taken, stray light may be acquired as a contaminant signal in the projection image recorded by the camera. The experiments in this section are therefore aimed toward describing the main sources of perturbation and considering the possibility of setting stray light-reducing protocols for improved FXG gel dosimetry. As the FXG gel dosimeter combines a low scattering attenuation gelatin matrix with an optical absorption dose contrast mechanism, evaluation of both scattering and absorbing solutions in the Vista scanner is required.

The fundamental relationship on which Feldkamp filtered back projection cone-beam reconstruction (Feldkamp *et al* 1984) is based is Beer's Law. This law states that for a light intensity I_o incident at the surface of a uniform substance of a linear attenuation coefficient μ, the attenuated light intensity I at some depth x in the substance is given by $I = I_o e^{-\mu x}$. The cone-beam reconstruction calculations presume that light travels in straight lines along cone-beam ray paths through the attenuating media. This 'ray path' condition generally holds

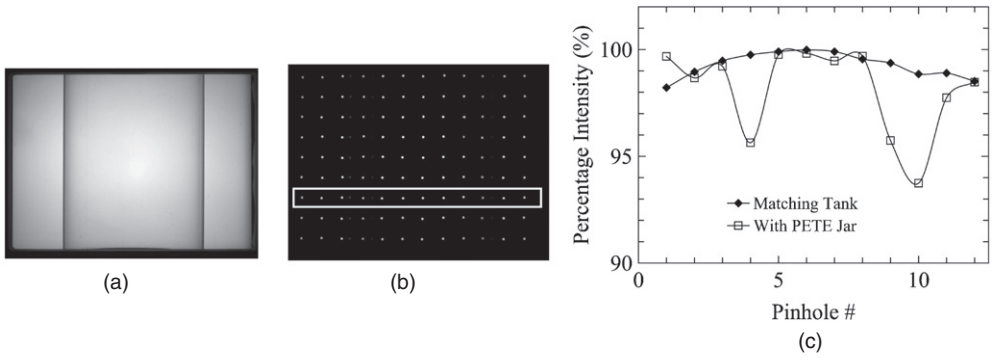

Figure 7. (a) Open field and (b) 2 mm diameter pinhole grid blocker projection images from the Vista scanner with a matching fluid-filled 1 L PETE jar in the matching tank. (c) Each pinhole blocker 'center pixel' intensity is extracted from one line of pinholes in the image (highlighted in figure 7(b)) and expressed as a percentage of open field intensity at the same pixel from the open field projection image. The plot shows the data from this line of pinholes with and without the matching tank-fluid-filled 1 L PETE jar in the tank. Fitted curves to the data are included to aid the eye.

true for the lens-based camera detector in the Vista scanner, as the camera optics only focus light onto the CCD chip that is traveling in tight ray bundles along cone-beam geometry ray paths toward the camera lens after exiting the attenuating media (Olding *et al* 2010).

One method of verifying the assumption of cone-beam geometry described in Olding *et al* (2010) involves the acquisition of two-dimensional (2D) percentage intensity maps from the Vista scanner. These maps are obtained through use of a 2 mm pinhole grid blocker inserted at the light source side of the matching tank. Each pinhole can be thought of as passing a tight ray bundle of light. Then, the intensity of light reaching the center pixel in the illuminated region at the detector with the pinhole blocker in place relative to the intensity reaching the same 'center' pixel under open field condition is effectively a measure of how much light reaching the camera is sourced in that ray bundle (or light cone). Similar stray light rejection schemes involving the use of physical collimators are also found in other CT geometries (Oldham and Kim 2004, Jirasek *et al* 2009). Figures 7(a) and (b) show open field and pinhole blocker images of a 12 wt% propylene glycol-in-water-filled 1 L PETE jar in the matching tank at 590 nm. The 0.8 mm thick aluminum matte-finished blocker used to obtain the image in figure 7(b) had 2 mm diameter pinholes, 11 mm (square) spacing between pinholes and was inserted at the light source side of the matching tank. Figure 7(c) shows the measurements along the line of blocker pinholes highlighted in figure 7(b), with and without the PETE jar inserted in the matching tank. The ratio varies less than 2% without the jar in place. When the jar is in the matching tank, a significant level of perturbation up to 4–6% near the jar walls is observed in the projection image.

The projection image data are increasingly perturbed when imaging scattering media (Olding *et al* 2010). To explore this effect, the 2 mm diameter pinhole blocker grid experiment described in figure 7 was repeated with a 5 wt% gelatin-in-water-filled jar (see figure 8). A bi-cubic spline function in MatLab was used to interpolate between measured grid points to obtain a 2D percentage map for the full projection image. A reduced mean 'jar region' percentage intensity value of ∼78% (figure 8(c)) is indicated. A series of increasing diameter single pinhole blockers (with the pinholes approximately centered in front of the jar) were

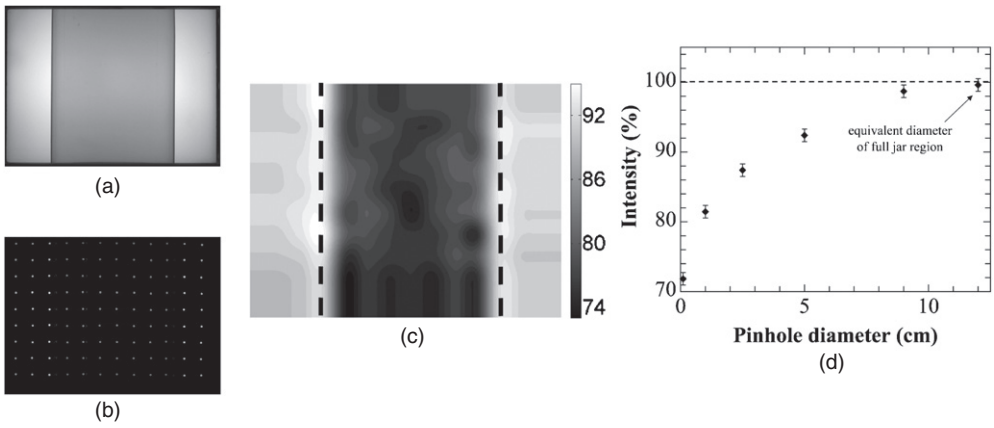

Figure 8. (a) Open field and (b) 2 mm diameter pinhole grid projection images from the Vista scanner with a 5 wt% gelatin-water filled 1 L PETE jar in the matching tank. (c) An interpolated percentage map is calculated from the measurements of peak pinhole intensity and open field intensity. The dotted lines show the jar edges. (d) Pinhole blocker 'center pixel' intensity values are extracted from the 'blocked' image and expressed as a percentage of open field intensity at the same pixel from the open field projection image. The varied diameter single pinhole blockers used in the measurements were placed at the light source side of the matching tank.

then inserted at the light source side of the matching tank in order to determine the extent of angled scatter intensity reaching each CCD camera pixel (figure 8(d)).

When the experiments are extended from a gelatin 'blank' to imaging an FXG dosimeter (i.e. an absorption dose contrast mechanism combined with a scattering gelatin matrix), slight variations are observed in the background stray light scatter 'wash' of dosimeters irradiated with different dose distributions. For example, percentage maps calculated from open field and 2 mm pinhole grid blocker projection images acquired at 590 nm using the Vista scanner are shown in figure 9 for (b) an un-irradiated FXG dosimeter, (d) a 200 cGy electron-beam-irradiated FXG dosimeter, and (f) a 200 cGy intensity-modulated radiation therapy (IMRT)-irradiated FXG dosimeter. The mean 'jar region' percentage values obtained for the three dosimeters were found to be 77.5%, 80.0% and 80.8%, respectively.

The question is: can the level of stray light perturbation be meaningfully reduced through a hardware adjustment or imaging protocol? It is difficult to assign meaningful protocols compensating for stray light sources inherent to the *dosimeter*, such as the jar interfaces or the scattering gel matrix. However, there are other sources of stray light in the system related to the *scanner*. Perhaps the simplest perturbation to manage (and the final focal point of this work) is contaminant stray light traveling through the low scattering matching fluid regions on either side of the jar. Diffuse light from this region can refract at the jar–fluid interface onto a primary ray path in the jar region of the transmission projection image. It is possible then that inserting custom blockers on either side of the jar could reduce the overall level of stray light perturbation.

To test this theory out, thick, black cardboard side blockers were inserted at the light source side of the matching tank, positioned 5 mm from the jar edges in the projection image (see figure 10(a)). Two reconstructed attenuation profiles across the jar region of a 1 L PETE jar containing the 1.48 mg L^{-1} absorbing solution are shown in figure 10(b), obtained with and without the side blockers in place in the Vista scanner (590 nm, 1.0 mm cubic voxel size). A projection image showing the placement of the side blockers is shown in the

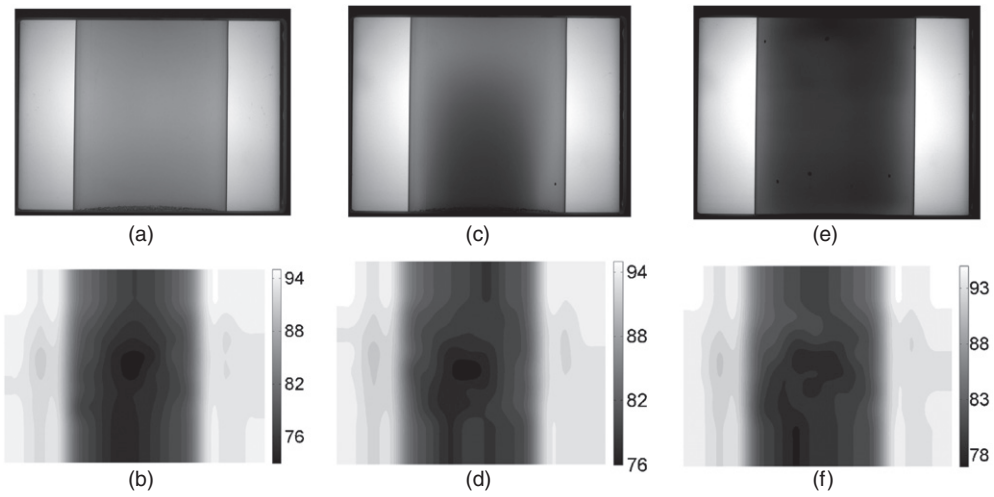

Figure 9. Projection images and 2 mm diameter pinhole blocker grid percentage maps for: (a), (b) an FXG dosimeter jar prior to irradiation with a calibration electron beam; (c), (d) a 200 cGy electron-beam-irradiated dosimeter and (e), (f) a test 200 cGy intensity-modulated radiation therapy (IMRT) delivery.

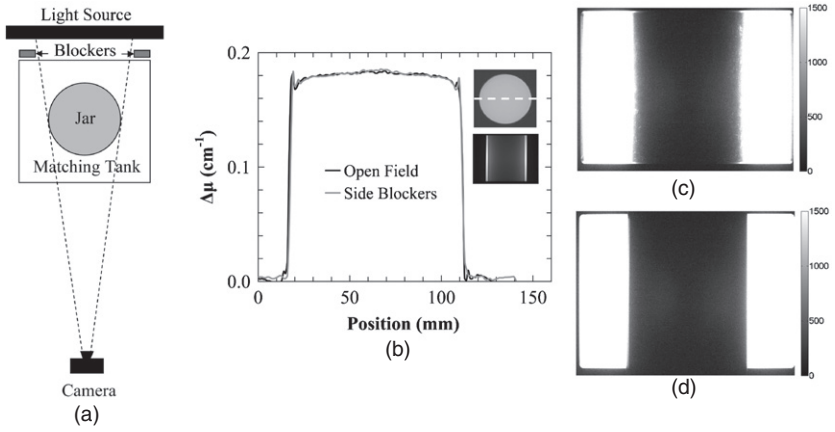

Figure 10. (a) Scanner setup with side blockers in place. (b) Profiles across the reconstructed images of a PETE jar containing 1.48 mg L^{-1} absorbing solution imaged on the Vista scanner, with and without side blockers at the light source side of the matching tank. Transmission projection images of the 1.48 mg L^{-1} absorbing solution with a blocker covering the jar region at (c) the light source side of, and (d) the camera side of the matching tank.

inset of figure 10(b). A jar region-sized cardboard blocker was then placed in front of the 1.48 mg L^{-1} absorbing solution at the light source side of the tank and a single projection image recorded (figure 10(c)). Evidence of stray light impingement is seen in the blocked jar region of the projection image, with a mean transmitted intensity of ∼450 arbitrary units (au) over the blocked jar region, ranging up to 1500 au near the jar walls. Dark field images recorded by the camera typically have a mean intensity of ∼25 au.

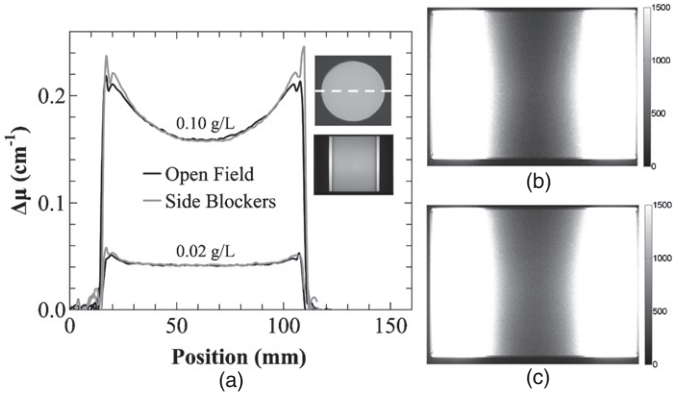

Figure 11. (a) Profiles across the reconstructed optical CT images of 1 L PETE jars containing the 0.02 and 0.10 g L^{-1} scattering solution imaged on the Vista scanner with and without side blockers at the light source side of the matching tank. Transmission projection images of: (b) 0.02 g L^{-1}, and (c) 0.10 g L^{-1} scattering solutions with a blocker covering the jar region at the light source side of matching tank.

A second 'blocked jar region' projection image was taken of the 1.48 mg L^{-1} absorbing solution with the blocker at the *camera side* of the matching tank (figure 10(d)). A small stray light perturbation was again observed in the blocked jar region with a mean intensity of 400 au ranging up to ∼900 au near the jar walls.

The stray light side blocker experiments were repeated under the same conditions as in figure 10(a), replacing the jar containing 1.48 mg L^{-1} absorbing solution with jars containing 0.02 and 0.10 g L^{-1} scattering solution. A slight reduction in reconstructed attenuation (that is particularly noticeable near the jar wall) is observed in the attenuation profiles without the side blockers in place (figure 11(a)). The effect is more clearly distinguished at the higher scattering concentration, where the ratio of stray light to primary transmitted light in the image is higher. Compared to the results in figure 10(c), greater stray light impingement is observed into the blocked jar region of the projection image, increasing with scatter concentration (see figures 11(b) and (c)).

3. Discussion

3.1. Scanner light source–detector stability

The reported decrease in a mean jar attenuation value of the calibration 0.1 g L^{-1} scatter solution as the scanner warms up (figure 1(a)) implies that the use of the Vista scanner projection image normalization region does not fully account for light source–detector variation. Taking a closer look at the mean intensity value in the jar region of the projection images from the first data scan (figure 1(b)), there is a significant drop in recorded intensity within the time frame of the scan. The Vista software normalization methodology accounts for inter-scan but not intra-scan variation, hence the change in response results in a drop in the reconstructed mean attenuation value.

The results show that the scanner light source essentially stabilizes within the first 1–2 h after the light panel is turned on (see independent photodiode measurements in figure 2(a)).

However, the sharp peak in recorded intensity observed after the light source is switched off for 5 min, then on again (figure 2(b)), indicates a 'cool down' instability in the output of the light source. The Vista scan software up to this point in its development incorporated a procedure of acquiring a dark field image as the last projection image in both reference and data scans by turning the light source off and leaving it off after the scan was completed. The software was henceforth modified to turn off the light source for the minimum amount of time required to acquire the dark field image, after which the light source was turned back on. This fast off–on operation was determined to have a negligible effect on the stability of the light source signal.

As most of the light source instability leading to a calculated reduction in attenuation occurs in the first 2 h of scanner warm-up, a protocol was established requiring: (1) a minimum of 2 h warm-up time prior to dosimeter scanning and (2) that the light source be kept on until completion of the last data scan. The software normalization routine is then able to effectively account for the possibility of a small, slow intensity variation over time suggested by the polynomial fit result from figure 2(a) (on the order of less than 1%). Without this correction, a slight baseline difference between mean light source intensity for the reference and data scans could be observed if the two scans are initiated during the peak and valley of the sinusoidal ripple respectively, or vice versa. Intra-scan light variations are small if the scanner warm up time protocol is employed, but it is conceivable that a further small improvement in measurement precision may be realized if individual projection image normalizations are incorporated in the reconstruction software.

3.2. Scan time constraints

The rate of FXG gel dosimeter development determined from the data presented in figure 3(b) is on par with the results reported by Kelly *et al* (1998). Since the rate of attenuation increase is roughly 3% per hour past the post-irradiation time of 30 min, and a typical 360°, 410 projection Vista scan takes 4–5 min, a mean increase in attenuation of approximately 0.25% occurs between start and end of the scan. Also, the time frame for the dose delivery of complicated treatment plans can be on the order of 5 min, which introduces an additional (intra-scan) variable into consideration for accurate dosimeter readout. The importance of a fast scan time is highlighted through this result. Dosimeter development is prohibitive to FXG dosimeter readout when using a point detection scheme-based optical scanner (with scan time on the order of hours), unless a time-based correction is employed.

In order to reduce the uncertainties introduced by diffusion, it is desirable to minimize the time between irradiation and imaging of the dosimeter. However, the rate of dose development is higher when imaging is performed before the 30 min mark (Kelly *et al* 1998), resulting in increased intra-scan attenuation variation. An approximate balance between these two parameters of dosimeter development and spatial dose integrity is found at 15–30 min post-irradiation. Given that the effects of diffusion are less significant away from dose gradients, but that dose development variation occurs through the entire dosimeter, a standard post-irradiation imaging time of 30 min was established for FXG dosimeter readout. Further reductions in scan time in the future may lead to reducing this time toward to the 15–20 min mark, which can be realistically achieved if the scanner is close in physical location to the irradiator in the clinic. Moving from a full scan over 360° to a half scan over 180° plus a fan angle of ∼12° to fully sample the Radon space (Kak and Slaney 2001) would be one logical step to take toward a shorter scan time, but with a tradeoff of decreased signal to noise. As in the case of dosimeter development, diffusion-related loss of spatial dose integrity over time also effectively prohibits the use of currently available point-detection optical scanners for

FXG dosimeter readout due to their slower scan times. However, it is possible that further development of fast first-generation systems, for example, the Krstajic and Doran (2007b) scanner, could achieve the reduced scan times required. The accurate assessment of time between irradiation and scanning is important enough to specify the standard post-irradiation wait time of 30 min prior optical cone-beam imaging to within ±30 s, which is readily accomplished.

3.3. Scan temperature constraints

In figure 5(a), an increase in transmitted intensity (i.e. decrease in attenuation) is observed in the projection images of the scattering solution as the solution warms up to room temperature. This effect is likely due the decreasing difference between the refractive indices of the solvent and scattering particles with increasing temperature (Franklin and Wang 2002). Given that the 3% increase in measured attenuation occurs over a range of 13 °C, a specification on scanner measurement temperature to within ±1 °C would control the uncertainty in measured attenuation due to the scattering gelatin matrix in the FXG gel dosimeter to ±0.25%. The measurements of the patent blue violet-based absorbing solution were essentially temperature independent (figure 5(a)). At this point one may be tempted to leave the scan temperature specification at ±1 °C. This would effectively minimize the temperature-dependent change in scatter attenuation from the gelatin matrix.

The results in figure 5(b) indicate, however, that unlike the patent blue violet dye solution, the FXG gel dosimeter exhibits significant optical attenuation temperature dependence. This thermochromic behavior is believed to be primarily caused by d-orbital spin state crossover of the ferric ion in the ferric ion–xylenol-orange dye complex with an increase in temperature (Wulfsberg 2000); this effect should be controlled for accurate dosimetry. The increase in attenuation with temperature was observed to be approximately 2.5% per degree Celsius (figure 6(a)) with or without the gelatin in a solution. This gives strong indication that the ferric ion–xylenol-orange dye complex is the primary source of attenuation change with temperature and that the dosimeter temperature should be strictly controlled to within the practical measurement limit of ±0.1 °C at the point of scanning. This result is more severe than that observed in a previous experiment, where the effect of temperature on un-irradiated FXG samples indicates an increase in the measured absorbance of ∼5% after warming the samples from 5 up to 30 °C (Bero and Kharita 2004). The two results are consistent, though, as the un-irradiated samples analyzed in Bero and Kharita's experiments primarily contain ferrous ions and only a minimal quantity of the thermochromic behavior-inducing ferric ion.

In order to accomplish the necessary degree of temperature control, two additional protocols were introduced in the scan procedure. First, on the day of irradiation, the refrigerated dosimeter jars are placed in a large covered 'holding' water bath (typically adjusted to between 20.0 and 21.0 ± 0.1 °C depending on the ambient temperature in the clinic) approximately 3–4 h before scanning to ensure temperature uniformity to within roughly ±0.2 °C in the gel dosimeter jar (figure 6(b)). The bath is covered to reduce ultraviolet light-driven reactions in the dosimeter. It is noteworthy that the presence of gelatin in a solution significantly slows down temperature equalization in the gel. Second, the temperature of the scanner matching bath is adjusted to the temperature of the holding bath (e.g. 20.0 ± 0.1 °C) immediately prior to the reference scan being performed. There are a few sources of heat in the scanner that can cause the matching bath to warm up over time (the stepper motor, the camera and to a small degree, the light source), so usually the matching bath needs to be cooled to the target temperature. To adjust the matching bath temperature, a PETE jar containing refrigerated

water or hot water is placed in the bath under low agitation stirring for a short period of time while monitoring the temperature until the target point is reached. The dosimeter is then inserted in the scanner matching bath and the bath temperature is recorded before and after the reference scan is completed. The dosimeter jar is returned to the covered holding bath until the time of irradiation and returned to the bath after irradiation until the time of the data scan measurement. These two protocols, when followed, significantly reduce observed fluctuations in the measurement that were previously assumed to be due to variation in batch preparation (chemical amounts, sensitivity, process of manufacture, etc).

One practice in gel dosimetry is to use a fitted dose-to-attenuation response obtained from a well-characterized delivery in a calibration FXG gel to regulate the readout of the gel being used as the study dosimeter. In this situation, the two dosimeters are prepared from the same gel batch in identically sized containers and stored under the same conditions (for example, see Babic *et al* (2008)). The absolute temperatures of the calibration and measurement dosimeters are not critical, as long as they are kept close to each other. Accomplishing this is relatively straightforward, as the two gels can be both placed in a temperature-controlled warming bath. Our experience is that the dosimeter temperature changes slowly when it is removed to in-air irradiation conditions. It would also be possible to correct the attenuation data by determining the attenuation-temperature dependence for the gel formulation in use and applying this to the attenuation data from each dosimeter based on a measurement of gel temperature. However, we have no need for this approach in our work.

3.4. Stray light reduction

The results presented in figure 7(c) clearly indicate that the refractive index (RI) mismatch-derived re-direction of light at jar wall interfaces is a primary source of stray light perturbation in the projection image data. There are two obvious approaches that could reduce this perturbation, both related to dosimeter manufacture. First, the PETE dosimeter jar could be replaced with another high optical clarity container derived from an acrylonitrile-based Barex^{TM}, or a polymethyl-methacrylate (PMMA)-based polymer. However, the RI value at a wavelength of 590 nm is only marginally different when the PETE jar with an RI of $\approx$1.58 (Shabana 2004) is replaced with Barex with an RI $\approx$ 1.51 (Islam *et al* 2003) or PMMA with an RI $\approx$ 1.49 (Groh and Zimmermann 1991). Given that the FXG gel has a refractive index of $\approx$1.345 at 590 nm, a slightly optically scattering fluoropolymer container material such as poly-tetrafluoroethylene (PTFE, e.g. Teflon^{TM}) with an RI $\approx$ 1.35 at 590 nm (Groh and Zimmermann 1991) would have to be used to provide a reasonable RI match between the gel and the jar material, as used in Babic *et al* (2008). Unfortunately, PTFE and its other fluoropolymer counterparts are comparatively expensive and are reasonably difficult to form into high quality, off-the-shelf dosimeter containers. Also, the question of whether optical scatter through the translucent PTFE container wall is more or less detrimental to stray light perturbation than refractive index-mismatch when using PETE has not been addressed to date.

The second option is to raise the RI of the gel and the matching tank fluid close to that of PETE. However, this involves a solvent replacement step that will compromise the water equivalence of the gel and may lead to deleterious changes in the radio-sensitivity of the Fricke-based dosimeter, as discussed previously (Olding *et al* 2010). A solid polyurethane radiochromic (PRESAGE^{TM}) dosimeter is available (Guo *et al* 2006a, 2006b) which does not require the use of a container and can be imaged using the cone-beam optical scanner. The lack of container wall-related stray light perturbations in the measurement is one advantage

of this system, as long as the non-tissue equivalence of the PRESAGE formulations (Brown *et al* 2008) is properly accounted for in the dosimetry.

As the RI mismatch-driven re-direction of light at jar wall interfaces is inherent to the physical structure of the dosimeter jar, it is difficult to set imaging protocols that will reduce this form of stray light perturbation in FXG gel dosimetry. Although it has not been confirmed, this effect is the likely source of bowing artifact observed in previous work with the Vista scanner (Jordan and Battista 2006, Olding *et al* 2010).

The second and perhaps the most significant source of stray light perturbation observed in cone-beam imaging of FXG gel dosimeters is angled scatter from the gelatin matrix. The results shown in figures 8(c) and (d) indicate that over 20% of the light arriving at each pixel throughout most of the jar region is scattered onto the primary ray path from a much larger region that is observed in the case of the absorbing solution. Contaminant light intensity at each detector pixel is scattered onto that pixel's primary cone-beam ray path from varied paths throughout the full jar volume (figure 8(d)). Without further consideration, this contaminant light intensity appears to compromise the measurement accuracy of the system. Note that the transmission map in figure 8(c) indicates some unexpected non-uniformity in the 2D stray light profile across the jar region of the image. This is partly due to optical effects/artifacts along the central axis of the jar and near the jar edges that have been previously identified and discussed (Jordan and Battista 2006, Babic *et al* 2009, Olding *et al* 2010). There is also noise present in the pinhole measurement, which in this case, was averaged over the 4 central pixels in each pinhole transmission region.

In another report, cone-beam optical CT-based FXG gel dosimetry has been shown to have good accuracy in the measurement of 3D dose (Babic *et al* (2008), see tables 1 and 2). To explain these results, two lines of thinking come into play. First, the scattering gelatin background does not significantly change during irradiation and hence there may be a partial cancellation in the low spatial variation scatter 'wash' background signal (see figure 8(c)) between reference and data scan, due to the fact that the ratio of reference to data scan projection intensities is taken during image reconstruction. This stray light perturbation will not be entirely cancelled in the reconstruction (due to the fact that the ratio is logarithmic in nature), but the resulting effect on reconstructed attenuation may be relatively small. Second, the dose response of the 'measurement' FXG gel dosimeter in Babic *et al* (2008) is calibrated using the attenuation-to-dose relationship obtained from a second well-characterized electron-beam-irradiated FXG gel dosimeter. If the angled scatter-based stray light perturbation is consistent between the calibration and measurement dosimeters, its effects may be calibrated out of the volume attenuation data. The results presented by Babic *et al* indicate that this is not entirely the case, but that a single value measured stray light correction applied to the projection data prior to image reconstruction appears to adequately manage this perturbation.

Looking at the projection image percentage maps presented in figure 9, the variation in mean scatter contribution between the three jars is seen to be relatively small. The differences are likely related to the degree to which scatter-sourced stray light is attenuated through optical absorption in the dosimeter. That is, stray light is attenuated least in the low absorbing un-irradiated dosimeter, more so in the electron-beam dosimeter and most in the highest absorbing IMRT dosimeter. There are no straightforward imaging protocols for reducing stray light perturbation due to angled scatter. The other Vista scanner imaging wavelength of 633 nm could be used (instead of 590 nm) to reduce the scatter contribution by $\sim$30%, as optical scattering through the dosimeter follows an approximate third- to fourth-order inverse wavelength dependence (Olding *et al* 2010). However, a new radio-sensitive dye would have to be identified, as the response of the iron–xylenol orange complex drops significantly at

633 nm compared to 590 nm (Kelly *et al* 1998). At present, the 590 nm imaging wavelength provides the best ratio of optical absorption response to scatter background signal.

The third source of stray light perturbation considered in this work is that due to the low scattering matching fluid on either side of the jar. The two attenuation profiles in figure 10(b) are observed to be very similar; this indicates that the light perturbation from the matching fluid is minimal when imaging absorbing media. This indicates that the overall stray light perturbation from the low scattering matching fluid regions on either side of the jar is minimal when imaging absorbing media. That is, most of the bowing artifact observed in the imaging of uniform absorbing media-filled jars (Jordan and Battista 2006, Olding *et al* 2010) is due to small angle re-direction of light traveling through the jar, not high angle re-direction of light originating from the regions on either side of the jar. Presumably, the stray light signal observed in the blocked jar region with the blocker at the light source side of the matching tank (figure 10(c)) is mostly cancelled in the ratio of reference to data images during image reconstruction, giving the matched profiles in figure 10(b).

The stray light signal recorded in the blocked jar region of the projection image when the blocker is placed at the camera side of the matching tank (figure 10(d)) requires further explanation. This form of stray light perturbation would not be expected to be derived from the negligible light scattering that occurs during travel through the air to the camera. The source of this effect is believed instead to be in the camera optics. In photography, there is a tendency for bright objects in the field of view to reduce the contrast everywhere within the image. This is termed 'veiling glare', a global illumination effect that arises from multiple scattering in the camera lens optics system (Williams 1999). The standard method for glare measurement involves photographing a dark target surrounded by bright illumination. For high attenuation absorbing solutions such as the 1.48 mg L^{-1} solution in question, the transmission projection image acquired by the camera fits this description well. It is possible that veiling glare could be a significant source of stray light-induced bowing artifact in the case where the absorbing solution has comparatively high optical absorbance compared to the surrounding matching tank fluid. One approach to reducing veiling glare would be to use a higher quality CCD camera-lens system in the scanner, to prevent multiple scattering in the lens optics. Another tactic to reduce this form of perturbation would be to replace the scanner light source. A variable intensity light source with high area intensity through the jar media and lower area intensity through the low scattering matching fluid regions on either side of the jar would act to both increase the dynamic range of the imaging system and decrease the bright-next-to-dark variability leading to veiling glare. Both of these hardware changes are considered to be outside the scope of this work.

When the absorbing media-filled jar is replaced with a scattering media-filled 1 L PETE jar in the matching tank, the management of high angle re-directed light originating from the regions on either side of the jar becomes more important. This is likely because this light can be further scattered by particles in the scattering media-filled jar onto a cone-beam primary ray path to the CCD detector. Referring to figure 11(a), the level of perturbation is sufficiently different between the reference jar containing matching tank fluid and the jars containing scattering media, that a slight reduction in reconstructed attenuation (which is particularly noticeable near the PETE jar wall) is observed in the attenuation profiles without the side blockers in place. The effect is more clearly distinguished at the higher scattering concentration, where the ratio of stray light to primary transmitted light in the image is higher. Since there is an observable difference in scattering systems, the question of whether the use of side blockers (baffles) in the Vista scanner (Babic *et al* 2008, 2009) should become standard practice in the imaging of FXG gel dosimeters (incorporating a scattering gelatin matrix) is important.

The 0.02 g L^{-1} scattering solution in figure 11 was chosen for evaluation because it is a close match in mean attenuation ($\sim$0.42 cm^{-1}) to a 5 wt% gelatin-in-water-filled 1 L PETE jar imaged at 590 nm ($\sim$0.45 cm^{-1}, see Olding *et al* (2010)), giving a quantitative sense of the stray light perturbation due to the gelatin matrix. The mean difference in reconstructed attenuation between the cross-jar data profiles in figure 11(a) was found to be less than 0.5% within the region extending from the jar center to 90% of its total radius. This represents the worst-case scenario for the magnitude of stray light perturbation, with little cancellation between the reference scan of the essentially non-scattering matching tank fluid and the data scan of the 0.02 g L^{-1} scattering solution. The FXG gel dosimeter, on the other hand, has a relatively unchanging gelatin matrix in both reference and data scans, and hence, should see greater cancellation of a gelatin scatter signal between the two scans. Thus, stray light perturbation sourced from the regions on either side of the jar should shift the reported attenuation by much less than 0.5%. Even with this in mind, the side blockers could be left in if there were no other considerations to account for. However, the insertion of these blockers prevents the use of the projection image normalization software correction discussed in section 1. The normalization region corrects for global differences in light source intensity that may be as much as 0.5–1.0% between the reference and data scan. The variability in light source–detector stability over time is comparatively a more significant source of uncertainty. Hence, the decision was made to adhere to the protocol of employing the standard projection image normalization routine, and forego the use of side blockers in the scanner. While a smaller normalization region could be obtained between the jar edge and the side blocker edge if side blockers were in place, the use of the larger standard normalization region is at present preferred. This preference is mostly due to the possibility of greater refractive light intensity variations near the dosimeter jar wall.

Overall, the results presented in this paper suggest some general conclusions for the implementation of optical CT-based gel dosimetry. First, most gel dosimeters will contain a gel-forming matrix material that is (a) inhomogeneous in a refractive index against the surrounding aqueous media, and (b) not well matched in a refractive index to the dosimeter container material. As these differences in refractive index are dependent on, and may be accentuated by, changes in temperature, it is prudent to have some form of temperature control in the optical imaging system. It is also important to establish temperature controls for the actual container size and gel recipe (for example, the weight percentage of gelatin in a solution changes the temperature response, see figure 6(b)) being used for the dosimetry.

Second, most gel dosimeters will exhibit some degree of ongoing dose development at the time of optical imaging. This suggests the implementation of a time control in the imaging. As a matter of standard practice, the post-irradiation time prior to imaging should be optimized for signal to noise, spatial dose integrity, and the speed of results (for each type of dosimeter). Beyond this, the goal should then be to complete the optical scan in as fast a time as possible to minimize intra-scan variations without compromising the quality of the raw intensity data.

Third, since the optical data will inherently be contaminated by stray light perturbation due to angled scatter from the gel-forming matrix material and refractive index mismatch at the container interface, the use of a second calibration gel dosimeter prepared in an identically sized container of the same material and filled with gel from the same batch is strongly indicated. The calibration and measurement dosimeter jars should then be irradiated and imaged under as closely matched time and temperature conditions as possible. The reasoning behind this conclusion is linked to the idea that most of the stray light perturbation will then be effectively cancelled in the dose-to-attenuation calibration relationship applied between the two dosimeters and the environmental variations between dosimeters will be minimized.

Table 1. Summary of key imaging protocols for FXG gel dosimetry.

Parameter	Recommended protocol
Scanner minimum warm up time	2 h prior to dosimeter reference scan
Dosimeter minimum warm up time	3 h in a 15–30 L 'holding tank' water bath at 20–23 °C prior to dosimeter reference scan
Matching tank solution temperature	Matched to holding tank water bath temperature within ± 0.2 °C in both reference and data scans
Pre-irradiation reference scan start time	Not critical as long as auto-oxidation occurring between the time of the reference and data scans is properly accounted for
Post-irradiation data scan start time	30 ± 0.5 min
Duration of scan	<5 min
Dark field image acquisition	At the end of each scan. Allow 5 min between scans for re-stabilization of the light source
Projection image normalization correction	Required
Side blockers for stray light reduction	Not required
Inter-jar attenuation-to-dose calibration (1)	Two identically-sized gel dosimeter jars from the same gel batch
Inter-jar attenuation-to-dose calibration (2)	Dosimeters warmed up in parallel in the holding tank water bath until the time of irradiation
Inter-jar attenuation-to-dose calibration (3)	Dosimeters irradiated within 10–60 min of each other, then returned to the holding tank water bath after irradiation until the time of optical scanning

Finally, table 1 summarizes the key suggestions for imaging with the present scanner hardware so as to minimize measurement errors.

4. Conclusions

Improved FXG dosimeter readout using the Vista cone-beam optical scanner can be realized through particular attention to the management of light source–detector stability, the wait time between irradiation and scan measurement, the overall scan time, and dosimeter scan temperature. Imaging protocols are established in this paper that increases the level of control in each of these areas without compromising the practicality of fast optical cone-beam FXG gel dosimeter readout. The identification of thermochromic behavior in the FXG gel, in particular, is an important step forward in improving its dosimetry. The largest sources of stray light perturbation in the system were identified as being due to angled scatter from the dosimeter gelatin matrix and refraction from the jar wall interfaces, both of which are better addressed through future work on dosimeter modification and an inter jar dose-to-attenuation calibration methodology, rather than by additional imaging protocols. The use of custom-side blockers for stray light reduction is not considered to be critical, and it prevents the use of an important software projection image normalization routine. Hence, specific imaging protocols were not realized in this work for the management of stray light perturbation in this scanner–dosimeter combination. Future effort in this regard should be primarily directed toward substitution of

the FXG dosimeter gelatin matrix and dosimeter container materials with stray-light reducing alternatives.

Acknowledgments

Research funding has been provided by the Cancer Centre of Southeastern Ontario and the Canadian Institutes of Health Research. The authors would like to acknowledge Kevin Jordan at the London Regional Cancer Centre for his helpful insight in identifying the effect of veiling glare in the CCD camera-based scanner.

References

Babic S, Battista J and Jordan K 2008 Three-dimensional dose verification for intensity-modulated radiation therapy in the radiological physics centre head-and-neck phantom using optical computed tomography scans of ferrous xylenol-orange gel dosimeters *Int. J. Radiat. Oncol. Biol. Phys.* **70** 1281–91

Babic S, McNiven A, Battista J and Jordan K 2009 Three-dimensional dosimetry of small megavoltage radiation fields using radiochromic gels and optical CT scanning *Phys. Med. Biol.* **54** 2463–81

Baldock C, Burford R P, Billingham N, Wagner G S, Patval S, Badawi R D and Keevil S F 1998 Experimental procedure for the manufacture and calibration of polyacrylamide gel (PAG) for magnetic resonance imaging (MRI) radiation dosimetry *Phys. Med. Biol.* **43** 695–702

Baldock C, Harris P J, Piercy A R and Healy B 2001 Experimental determination of the diffusion coefficient in two-dimensions in ferrous sulphate gels using the finite element method *Australas. Phys. Eng. Sci. Med.* **24** 19–30

Baldock C, Murry P and Kron T 1999 Uncertainty analysis in polymer gel dosimetry *Phys. Med. Biol.* **44** N243–6

Bero M A and Kharita M H 2004 Effects of ambient temperature on the FXG radiochromic gels used for 3-D dosimetry *J. Phys.: Conf. Ser.* **3** 236–9

Bosi S G, Brown S, Sarabipour S, De Deene Y and Baldock C 2009 Modelling optical scattering artefacts for varying pathlength in a gel dosimeter phantom *Phys. Med. Biol.* **54** 275–83

Bosi S, Naseri P, Puran A, Davies J and Baldock C 2007 Initial investigation of a novel light-scattering gel phantom for evaluation of optical CT scanners for radiotherapy gel dosimetry *Phys. Med. Biol.* **52** 2893–903

Brown S, Venning A, De Deene Y, Vial P, Oliver L, Adamovics J and Baldock C 2008 Radiological properties of the PRESAGE and PAGAT polymer dosimeters *Appl. Radiat. Isot.* **66** 1970–4

De Deene Y 2004 Fundamentals of MRI measurements for gel dosimetry *J. Phys.: Conf. Ser.* **3** 87–114

De Deene Y and Baldock C 2002 Optimization of multiple spin-echo sequences for 3D polymer gel dosimetry *Phys. Med. Biol.* **47** 3117–41

De Deene Y, Hurley C, Venning A, Vergote K, Mather M, Healy B J and Baldock C 2002 A basic study of some normoxic polymer gel dosimeters *Phys. Med. Biol.* **47** 3441–63

De Deene Y, Vergote K, Claeys C and De Wagter C 2006 The fundamental radiation properties of normoxic polymer gel dosimeters: a comparison between a methacrylic acid based gel and acrylamide based gels *Phys. Med. Biol.* **51** 653–73

Doran S 2009 The history and principles of optical computed tomography for scanning 3-D radiation dosimeters: 2008 update *J. Phys.: Conf. Ser.* **164** 012020

Doran S J, Koerkamp K K, Bero M A, Jenneson P, Morton E J and Gilboy W B 2001 A CCD-based optical CT scanner for high-resolution 3D imaging of radiation dose distributions: equipment specifications, optical simulations and preliminary results *Phys. Med. Biol.* **46** 3191–213

Feldkamp L A, Davis L C and Kress J W 1984 Practical cone-beam algorithm *J. Opt. Soc. Am.* **1** 612–9

Franklin J and Wang Z Y 2002 Refractive index matching: a general method for enhancing the optical clarity of a hydrogel matrix *Chem. Mater.* **14** 4487–9

Gore J C, Kang Y S and Schulz R J 1984 Measurement of radiation dose distributions by nuclear magnetic resonance (NMR) imaging *Phys. Med. Biol.* **29** 1189–97

Gore J C, Ranade M, Maryanski M J and Schulz R J 1996 Radiation dose distributions in three dimensions from tomographic optical density scanning of polymer gels: I. Development of an optical scanner *Phys. Med. Biol.* **41** 2695–704

Groh W and Zimmermann A 1991 What is the lowest refractive index of an organic polymer? *Macromolecules* **24** 6660–3

Guo P, Adamovics J and Oldham M 2006a A practical three-dimensional dosimetry system for radiation therapy *Med. Phys.* **33** 3962–72

Guo P Y, Adamovics J A and Oldham M 2006b Characterization of a new radiochromic three-dimensional dosimeter *Med. Phys.* **33** 1338–45

Harris P J, Piercy A and Baldock C 1996 A method for determining the diffusion coefficient in Fe(II/III) radiation dosimetry gels using finite elements *Phys. Med. Biol.* **41** 1745–53

Islam K T, Dempsey J F, Ranade M K, Maryanski M J and Low D A 2003 Initial evaluation of commercial optical CT-based 3D gel dosimeter *Med. Phys.* **30** 2159–68

Jirasek A, Rudko D and Wells D 2009 A prototype fan-beam optical CT scanner for polymer gel dosimetry *J. Phys.: Conf. Ser.* **164** 012025

Jordan K and Battista J 2006 Linearity and image uniformity of the Vista^{TM} optical CT scanner *J. Phys.: Conf. Ser.* **56** 217–20

Jordan K and Battista J 2009 Scatter measurements for optical cone-beam computed tomography *J. Phys.: Conf. Ser.* **164** 012028

Kak A C and Slaney M 2001 *Principles of Computerized Tomographic Imaging* (Philadelphia, PA: Society for Industrial and Applied Mathematics) p 327

Kelly B G, Jordan K J and Battista J J 1998 Optical CT reconstruction of 3D dose distributions using the ferrous-benzoic-xylenol (FBX) gel dosimeter *Med. Phys.* **25** 1741–50

Krstajic N and Doran S J 2006 Focusing optics of a parallel beam CCD optical tomography apparatus for 3D radiation gel dosimetry *Phys. Med. Biol.* **51** 2055–75

Krstajic N and Doran S J 2007a Characterization of a parallel-beam CCD optical-CT apparatus for 3D radiation dosimetry *Phys. Med. Biol.* **52** 3693–713

Krstajic N and Doran S J 2007b Fast laser scanning optical-CT apparatus for 3D radiation dosimetry *Phys. Med. Biol.* **52** N257–63

Lopatiuk-Tirpak O, Langen K M, Meeks S L, Kupelian P A, Zeidan O A and Maryanski M J 2008 Performance evaluation of an improved optical computed tomography polymer gel dosimeter system for 3D dose verification of static and dynamic phantom deliveries *Med. Phys.* **35** 3847–59

Oldham M and Kim L 2004 Optical-CT gel-dosimetry: II. Optical artifacts and geometrical distortion *Med. Phys.* **31** 1093–104

Oldham M, Siewerdsen J H, Shetty A and Jaffray D A 2001 High resolution gel-dosimetry by optical-CT and MR scanning *Med. Phys.* **28** 1436–45

Olding T, Holmes O and Schreiner L J 2010 Cone beam optical computed tomography for gel dosimetry I: scanner characterization *Phys. Med. Biol.* **55** 2819–40

Olsson L E, Fransson A, Ericsson A and Mattsson S 1990 MR imaging of absorbed dose distributions for radiotherapy using ferrous sulphate gels *Phys. Med. Biol.* **35** 1623–31

Rae W I, Willemse C A, Lotter M G, Engelbrecht J S and Swarts J C 1996 Chelator effect on ion diffusion in ferrous-sulfate-doped gelatin gel dosimeters as analyzed by MRI *Med. Phys.* **23** 15–23

Schreiner L J and Olding T 2009 Gel Dosimetry *AAPM Medical Physics Monograph No. 34: Clinical Dosimetry Measurements in Radiotherapy* ed D W Rogers and J E Cygler (Madison, WI: Medical Physics Publishing)

Shabana H M 2004 Refractive index-structure correlation in chemically treated polyethylene terephthalate fibres *Polym. Test.* **23** 291–7

Tarte B J and van Doorn T 1993 Optical scanning of ferrous sulphate gels for radiotherapy treatment dosimetry *APSEM/BECON Australasian Conf. on Physical Science and Engineering in Medicine/Biomedical Engineering* p 126

Tarte B J and van Doorn T 1995 Laser based tomographic scanning of gel volumes for applications in ionising radiation dosimetry *10th Conf. of the Australasian Optical Society (University of Queensland, Australia)*

Taylor M L, Franich R D, Johnston P N, Millar R M and Trapp J V 2007 Systematic variations in polymer gel dosimeter calibration due to container influence and deviations from water equivalence *Phys. Med. Biol.* **52** 3991–4005

Taylor M L, Franich R D, Trapp J V and Johnston P N 2009 A comparative study of the effect of calibration conditions on the water equivalence of a range of gel dosimeters *IEEE Trans. Nucl. Sci.* **56** 429–36

Williams T J 1999 Veiling glare *The Optical Transfer Function of Imaging Systems* (Bristol, UK: Institute of Physics Publishing) p 405

Wolodzko J G, Marsden C and Appleby A 1999 CCD imaging for optical tomography of gel radiation dosimeters *Med. Phys.* **26** 2508–13

Wulfsberg G 2000 *Inorganic Chemistry* (Sausalito, CA: University Science Books) p 368